TEL AVIV UNIVERSITY אוניברסיטת תל-אביב

RAYMOND AND BEVERLY SACKLER
FACULTY OF EXACT SCIENCES
SCHOOL OF PHYSICS & ASTRONOMY

הפקולטה למדעים מדוייקים
ע"ש ריימונד ובברלי סאקלר
בית הספר לפיסיקה ואסטרונומיה

Supernova Counts in Deep *Hubble Space Telescope* Fields

THESIS SUBMITTED FOR THE M.Sc. DEGREE
AT TEL-AVIV UNIVERSITY
SCHOOL OF PHYSICS AND ASTRONOMY

by

Keren Sharon

This work was carried out under the supervision of
Prof. Dan Maoz

September 2003

Contents

Abstract

Little is known about the properties of high-redshift SNe. While much progress has been made in recent years in finding distant Type Ia SNe for Hubble diagram purposes, their environments, rates, typical brightness, progenitors and explosion mechanisms are currently weakly constrained by observations. As for distant core-collapse SNe, only a few such SNe have been discovered to date, and systematic surveys that can constrain their rates have not been carried out. The goal of this work, is to conduct a systematic survey for high-z SNe in order to characterize their properties. It is a pilot study for larger surveys, planned or currently under way. We have searched for high-redshift supernova candidates in multiple, deep Hubble Space Telescope (*HST*) archival images of nine galaxy clusters, and in the Groth Survey Strip (GSS). We detect ten apparent SNe, with $21.6 \leq I_{814} \leq 28.4$ mag, in a total area of ~ 270 arcmin^2. Of the six SNe discovered in the galaxy-cluster sample, two are associated with cluster galaxies (at redshifts $z = 0.18$ and $z = 0.83$), three are probably in galaxies not in the clusters (at $z = 0.49$, $z = 0.60$, and $z = 0.98$), and one is at unknown z. Three of the four SN candidates discovered in the GSS are also at unknown redshifts, and one is possibly at $z = 1.45$. After accounting for observational efficiencies and uncertainties (statistical and systematic) we compare our observed counts of field SNe (i.e., non-cluster SNe of all types) to recent model predictions. The observed field count is $N \leq 3$ SN with $I_{814} \leq 26$ mag, and $5 \leq N \leq 7$ SNe with $I_{814} \leq 27$ mag. These counts rule out one model, and are only marginally consistent with another. Since the counts at these magnitudes are likely dominated by type-II SNe, our observations suggest obscuration of distant SNe-II, or a SN-II luminosity distribution devoid of a large high-luminosity tail. Our findings rely on a small number of events, and are subject to large uncertainties due to small number statistics. Similar analysis of larger datasets, expected to arise from surveys that are planned or already operative, would yield SN counts with higher precision, and can provide stronger limits on SN properties.

Chapter 1

Introduction

Supernovae (SNe) are the violent explosions of stars, occurring roughly once a century in a given galaxy. The typical energy released in such an explosion is of order the binding energy of a neutron star, $\sim 10^{53}$ erg, or the thermonuclear consumption yield of a star, $0.007 M_{\odot} c^2 \sim 10^{52}$ erg. Although only a small fraction of this energy is in electromagnetic radiation, the radiation is released on a timescale of weeks, and hence the luminosity of a SN event can briefly rival an entire galaxy. There are several types of SN, which differ both in their observational properties and in their physical origins, as will be described below. The main distinction between SNe and other cataclysmic variables is that the progenitors change their stellar character, i.e., a massive star or a white dwarf disintegrate, leaving a neutron star, a black hole, or nothing, behind. One of the open interesting questions in astronomy, is the identification of the progenitors of each type of SN. Direct observational detection of the pre-SN star, exists only in two cases: SN1987A, and SN1993J.

Type Ia SNe are extensively used as distance indicators in cosmological studies, owing to their brightness and homogeneity. SNe of all types also play an important role in the chemical evolution of the Universe, as these energetic explosions are the only known sites for the synthesis of all elements heavier than oxygen.

1.1 Supernova Types

SNe are traditionally categorized into taxonomic subtypes. The two main classes are Type I SNe, which do not show hydrogen lines in their spectra, and Type II SNe with prominent hydrogen lines (Minkowski, 1941). Each type is further sorted into several subtypes, defined by the presence or absence of absorption and emission features of certain elements in their early-time optical spectra, and by the shape of their lightcurves.

A more physical categorization of SNe arises from the current understanding of their origin and explosion mechanisms. SNe Ia, a sub-type of SNe I, are believed to be associated with the thermonuclear explosion of a white dwarf (WD) triggered by accretion from, or merger with, a binary companion. However, the exact progenitors and evolutionary process leading to the formation of SNe Ia are not known. All other types of SNe are likely the outcome of the core collapse of massive stars. The main evidence for this is that core-collapse SNe are always closely associated with the arms of spiral galaxies and star forming regions, while SNe Ia can be found in all types of galaxies.

SN events probe the star formation history (SFH) of the Universe. A burst of star formation is followed by the core collapse of the short-lived, massive stars, within $\sim 10^7$ years. The time delay between star formation and explosion of some members of the stellar population as SNe Ia is not well determined. Some observational constraints have been recently derived by Gal-Yam & Maoz (2003) and Maoz & Gal-Yam (2003).

We briefly describe each type of SN below.

1.1.1 Core Collapse Supernovae

The detailed process of collapse in SNe is still a difficult theoretical problem. When the nuclear reactions in the cores of massive ($> 8M_\odot$) stars cease, the cores become unstable and collapse, forming a neutron star or a black hole, while releasing the gravitational energy in several forms. Most of the energy ($\sim 10^{53}$ ergs) is carried away by neutrinos, as had been demonstrated directly in the case of SN1987A. About 1% of the energy is kinetic, and only about 10^{-4} of the energy is released as electromagnetic radiation. In cases where the explosion occurs within a thick circumstellar medium (CSM), the interaction between the SN ejecta and the surrounding CSM may convert kinetic energy into additional radiation.

Type Ib and Ic Supernovae

The spectra of SNe Ib show strong He I $\lambda\lambda 4471, 5876, 6678$ and 7056 lines, weak or absent Si II $\lambda\lambda 6347, 6371$ lines, and no hydrogen lines. SNe Ic show absorption lines of Ca II and O I, weak or absent H and He lines, and no Si II $\lambda\lambda 6347, 6371$ lines. Apart from the He I lines, the spectra of these two types are usually similar. Moreover, intermediate cases exist, showing similarity to both types, and suggest a continuous transition between the types.

The lack of hydrogen in the spectra suggests that the progenitors of these types of SNe are massive stars that have lost most of their H/He-rich envelopes to winds or have transferred them to a binary companion, prior to the explosion. Most of the collapse energy deposited in the envelopes generates adiabatic expansion, and the optical lightcurve is powered by radioactive heating. The common temporal behavior of the visible emission of SNe Ib and Ic is a brightening phase during 2-3 weeks, followed by a fast dimming during $\sim$30 days and a slow decline stage. Figure 1.1 shows a schematic lightcurve for each type of SN. The attributes of the lightcurve (peak and width) depend on the amount of ^{56}Ni synthesized in the explosion, the envelope mass, and the expansion velocity. These objects are usually radio loud, owing to a strong interaction with the CSM which was probably stripped from the progenitor prior to the explosion.

Another sub-class of SNe Ic showing high expansion velocities in their early-time spectra was recently identified (e.g., SN 1998bw, Galama et al. 1998; SN 2002ap, Gal-Yam et al. 2002, Foley et al. 2003). Some gamma-ray bursts (GRBs) have been shown to be associated with such SNe (Stanek et al. 2003). This small group of SNe is referred to as SN1998bw-like events. They are characterized by featureless spectra, with wide bumps indicating extremely high expansion velocities, resulting in strong Doppler broadening and blending of spectral lines. Their lightcurves differ in widths and luminosities, and are similar to those of SNe Ic in their shape.

Type II Supernovae

Type II SNe are identified by the obvious presence of hydrogen Balmer lines in their optical spectra. The spectra and lightcurves of Type II SNe show great diversity, probably due to differences in the masses of the progenitors and the ejecta, expansion velocities, and the environments in which the explosions occur. Other elements commonly detectable in Type II spectra are He, Ca, Fe, and other iron-group elements.

Type II-P and II-L Supernovae – Types II-P (P stands for plateau) and II-L (linear) are "classical" Type II SNe (i.e., showing broad and strong Balmer line in emission), which differ by their temporal behavior. The lightcurve of SNe II-P stops declining shortly after maximum, stays nearly constant for about 2-3 months, and then rapidly declines again. A class of very underluminous SNe, such as SN 1987A, are believed to be extreme cases of the II-P sub-type (e.g., Nomoto et al. 2003, Zampieri et al. 2003). The magnitude of SNe II-L, on the other hand, declines linearly with time.

The optical spectra of Type II SNe are dominated by Balmer lines exhibiting P-Cygni profiles, typical of an expanding atmosphere, and show a diversity of line widths, implying differences in expansion velocities. The low luminosities at radio frequencies imply that this kind of explosions occurs in relatively low-density environments.

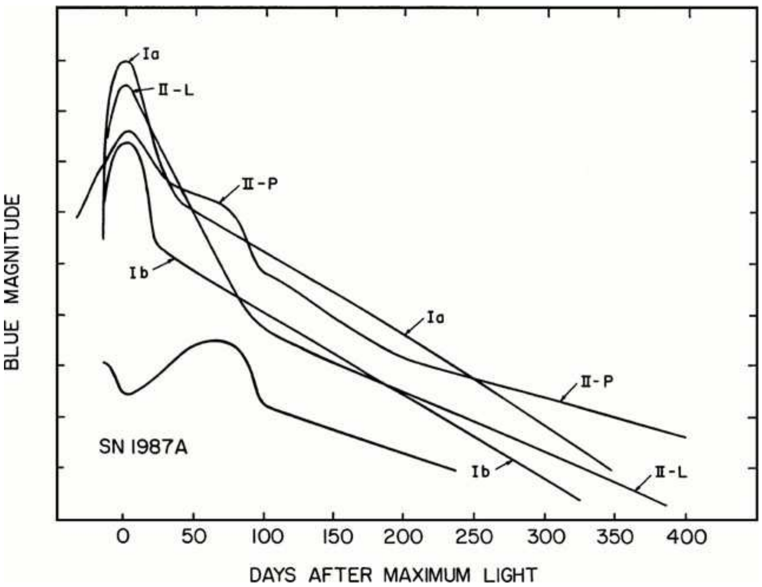

Fig. 1.1.— Schematic light curves for SNe of Types Ia, Ib, II-L, II-P, and SN 1987A. The curve for SNe Ib includes SNe Ic as well, and represents an average. For SNe II-L, SNe 1979C and 1980K are used, but these might be unusually luminous. From Filippenko (1997).

Type IIb Supernovae – SNe IIb resemble classical Type II's in their early time spectra (i.e., with prominent H lines), but their later-time spectra appear more and more like those of Type Ib/c. This is interpreted as due to a very low-mass H-envelope. They are believed to be the link between Type I and Type II core collapse SNe, implying that core collapse SNe exhibit a continuous spectroscopic sequence, II-P-II-L-IIb-Ib-Ic, which reflects the ability of the SN progenitors to retain their H-rich envelopes prior to explosion.

Type IIn Supernovae – SNe IIn show narrow lines in their spectra, believed to be associated with a strong interaction with a dense CSM. The dominant features are narrow Hα emission profiles, and a lack of absorption in the Balmer lines. The densities of the CSM and the ejecta determine the characteristics of the emitted radiation.

Relative abundances The relative fractions (f) of each type of SN within the SN population are not well determined. Commonly cited ratios (e.g., Cappellaro et al. 1993, 1997, 1999), which are based on observations of the nearby Universe, are $f(II\text{-}P) \sim f(II\text{-}L)$, $f(II) = f(II\text{-}P)+f(II\text{-}L)$, $f(Ib/c) \simeq 0.3f(II)$, and $f(IIn) \simeq 0.05f(II)$.

1.1.2 Type Ia Supernovae

SNe Ia are believed to be thermonuclear disruptions of accreting WDs, resulting in very luminous explosions.

Although SNe Ia are usually ~ 10 times brighter than the most frequently discovered core collapse SNe, the total energy released in the thermonuclear explosion ($\sim 10^{51}$ erg) is two orders of magnitude lower, since most of the energy produced by core collapse SNe is carried away by neutrinos.

Two explosion scenarios are usually considered in the literature. In the first, the accreting white dwarf reaches the Chandrasekhar mass, igniting the carbon in its core. In the second, the carbon is ignited at sub-Chandrasekhar masses, as a result of a compression of the core induced by the ignition of the accreted helium layer near the surface of the WD.

The optical spectra of Type Ia SNe are usually quite homogeneous, as well as the shapes of their lightcurves. Apart from the lack of hydrogen, SNe Ia spectra are characterized by strong absorption lines of Si II $\lambda\lambda 6347, 6371$. Other absorption lines of intermediate mass elements are observed during the peak, and strong emission of Fe III and Fe II dominates the spectra several months later. The optical lightcurve is similar to that of other SN I types. The luminosity declines during $\sim$20 days after maximum brightness at about 0.065 mag day^{-1}, followed by a slower, constant decline rate of about 0.015 mag day^{-1} starting about 50 days after the peak. Observations at other wavelengths reveal a secondary peak in the infrared and the I-band some 20-30 days after the visual maximum. There is a small luminosity dispersion at maximum, which is strongly correlated with lightcurve shape, allowing the use of SNe Ia as distance indicators. The maximum brightness is, again, linked to the amount of ^{56}Ni synthesized in the explosion.

1.2 Supernova Surveys

Early searches for extragalactic SNe were mostly targeted at the nearby Universe (e.g., Hubble & Humason 1931; Zwicky, Humason & Gates 1960). These searches relied on photographic and visual observations, and resulted in the discovery of several SNe each year. In the last few decades, with the emerging of the wide-field CCD imaging technology and the advances made in computing capabilities, SN searches have become more systematic, allowing the automatic discovery of tens to hundreds of SNe a year, in all redshift ranges. Nearby galaxies are monitored for SNe by several programs (e.g., Li et al. 1996; Treffers et al. 1997; Filippenko et al. 2001; Dimai 2001; Qiu & Hu 2001), as well as wide-field, moderately deep surveys (e.g., Reiss et al. 1998; Gal-Yam & Maoz 1999; Gal-Yam et al. 2003; Hardin et al. 2000; Schaefer 2000).

The search for distant supernovae (SNe) has been revolutionized in the last few years by two cosmology-oriented groups, the Supernova Cosmology Project (SCP; Perlmutter et al. 1997), and the High-z SN Search Team (Schmidt et al. 1998). Both groups have discovered hundreds of distant SNe Ia with redshifts up to $z \sim 1$, for use as standard candles. The Hubble diagram based on analysis of these data shows evidence for an accelerating Universe, possibly driven by a positive cosmological constant (Riess et al. 1998; Perlmutter et al. 1999; Tonry et al. 2003). Two likely high-z SNe have also been discovered in a repeated observation with the *Hubble Space Telescope* (*HST*) of the Hubble Deep Field (HDF; Gilliland, Nugent, & Phillips 1999). One of these SNe has been shown by Riess et al. (2001) to be a type-Ia at $z = 1.7$, at an epoch before the transition from universal deceleration to acceleration. More recently, 42 high-z SNe have been identified by the Great Observatories Origins Deep Survey (GOODS), 22 of them at $z > 1$ in deep images covering ~ 170 arcmin^2 fields, using the Advanced Camera for Surveys (ACS) onboard *HST* (Strolger et al. 2003, Riess et al. 2003). These works demonstrate that deep *HST* observations are an efficient way to find high-z SNe, with the high angular resolution and low sky background compensating for the small field of view.

1.3 Objectives of This Work

Apart from the use of SNe Ia as standard candles, it is important to find and characterize distant SNe of all types. SN rates as a function of redshift probe SFH, the physical mechanisms leading to SN-Ia explosions, and the cosmological parameters (Jorgensen et al. 1997; Sadat et al. 1998; Ruiz-Lapuente & Canal 1998; Madau, Della Valle, & Panagia 1998; Yungelson & Livio 2000; Gal-Yam & Maoz 2003). Furthermore, even in the absence of redshift information, SN number counts (i.e., the number of SNe visible per unit sky area at a given time) as a function of limiting magnitude can provide valuable constraints (Dahlén & Fransson 1999, hereafter DF; Sullivan et al. 2000, hereafter S2000; Gal-Yam, Maoz & Sharon 2002).

The environments and rates of high-z SNe Ia are fairly constrained by observations. The new search and follow-up technique that was developed by the SCP provides well-controlled search conditions, making it possible to measure the rate of occurrence of distant SNe (Pain et al. 1996; 2002). Sullivan et al. (2003) have studied the dependence of the distant type Ia SN properties on host galaxy environments, using the same database.

However, the situation is different for core-collapse SNe. Only a few high-z core-collapse SNe have been discovered to date, and even those few discovered by the SN-Ia-oriented surveys are poorly studied, being not the main science drivers of these programs. Furthermore, systematic surveys that can constrain the properties of core-collapse SNe have not been conducted. Thus, little is known about their environments, rates, typical brightness, progenitors and explosion mechanisms.

The goal of this work is to conduct a survey for high-z SNe, of all types, in order to characterize their properties. The high-z SN rates depends on the SFH, the intrinsic SN luminosity function, and extinction by dust. By measuring SN rates or counts, we can constrain combinations of these parameters, and examine the validity of the assumptions upon which current theoretical models are based. In this virtually unexplored field, our work is a pilot study for larger surveys, planned or currently underway.

In this work, we describe our search for SNe in duplicate *HST* observations. We first surveyed a sample of deep galaxy cluster fields. In this sample, we discovered six SNe, two or three of which were related to cluster-member galaxies, while the rest were probably background or foreground events. We used the SNe *within* the clusters to derive SN Ia rates in galaxy clusters (reported in Gal-Yam, Maoz, & Sharon, 2002). The *non-cluster* SNe in the galaxy-cluster fields turned out to be useful probes of the high-z SN population. In Gal-Yam et al. (2002) we also carried out a first comparison of the counts of the field SNe to model predictions. However, this comparison was based on only two or three SNe.

We therefore initiated a more comprehensive search for field SNe in large area of blank sky (the Groth Survey Strip, GSS), in order to increase the number of events and improve the SN statistics. Four SNe were discovered in the GSS. The archival search and the analysis of the images are outlined in § 2. In § 3, we describe the six SNe found in the galaxy-cluster sample, and the four SN candidates detected in the GSS data. We test our detection efficiency in § 4, and in § 5 we argue that all these variable objects are most likely SNe. Combining the four GSS SN candidate with the non-cluster events, previously reported in Gal-Yam et al. (2002), we test the theoretical predictions for SN number counts in blank fields. The analysis in this work extends our previous analysis in terms of methodology as well as the larger SN numbers. This is described in § 6.

Where applicable, we assume a flat cosmology with parameters $\Omega_m = 0.3$ and $\Omega_\Lambda = 0.7$, and use h_{50} to denote the Hubble parameter in units of 50 km s^{-1} Mpc^{-1}.

We report our observations using the AB magnitude system, in which the magnitude in a band b centered at wavelength λ [nm] is $b_\lambda = -48.6 - 2.5 \times \log f_\nu$, where f_ν is the flux density at frequency ν in erg s^{-1} cm^{-2} Hz^{-1}.

Chapter 2

Data acquisition and analysis

2.1 Hubble Space Telescope

The Hubble Space Telescope (*HST*) is a 2.4-meter reflecting telescope in low-Earth orbit (600 kilometers), operative since April 1990. *HST*'s location above the Earth's atmosphere provides high resolution, of approximately $0.05''$, for visible light, which is still unmatched by ground-based telescopes (with adaptive optics technology).

All the fields used in this work were imaged by the Wide Field Planetary Camera 2 (WFPC2). The WFPC2 field of view is divided into four detectors, each consisting of an 800×800 pixel CCD. Three CCDs comprise the Wide Field Camera (WFC), with an image scale of $0.0996''$ per pixel (f/12.9) and an $1.5' \times 1.5'$ "L" shaped field of view (see Fig. 2.1). The fourth CCD (Planetary Camera, PC) has a resolution of $0.0455''$ per pixel (f/28.3), which translates to a field of view of $35'' \times 35''$.

HST is subject to the impact of cosmic rays (CRs) and protons from the Earth's radiation belts. The showers of secondary particles produced when these are scattered by the spacecraft lead to "cosmic ray events" occurring at an average rate of $1.8\ \mathrm{s}^{-1}$ per detector. These events deposit varying amounts of charge, in one or more pixels, thus invalidating the data stored in these pixels. Long science observations are therefore usually broken into at least two exposures, to enable CR identification and rejection.

The point-spread function of the telescope and camera optics is undersampled by a factor of 2 by the PC pixels at visual wavelengths, and by a factor of four by the WF pixels. Some of the lost sampling can be recovered by non integer dithering, i.e., introducing sub-pixel offsets between sub-exposures of each observation.

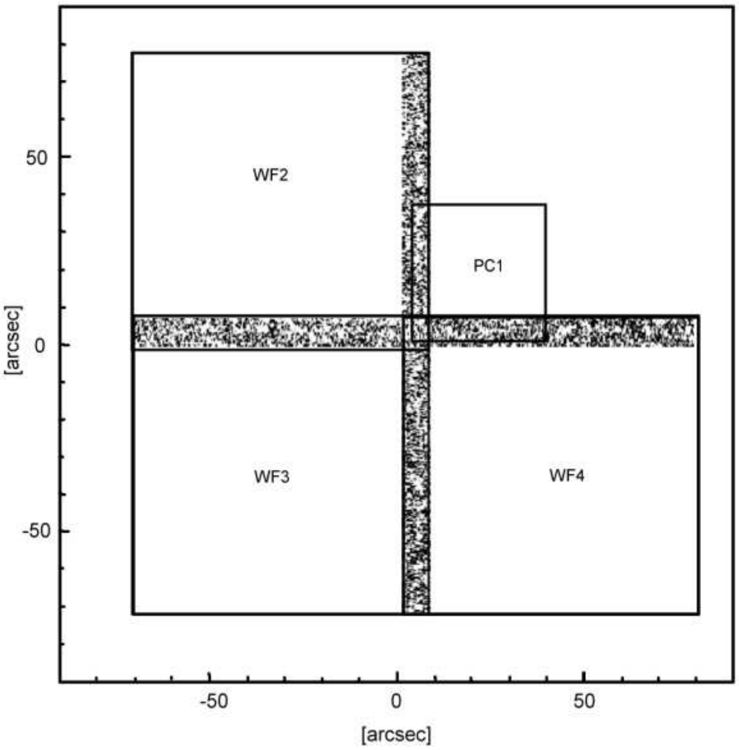

Fig. 2.1.— WFPC2 field of view

The orientation of the field (i.e., rotation angle of the camera) depends on the pointing direction and observation epoch, since the spatial orientation of the satellite is restricted by the direction to the Sun and the availability of guide stars. The peculiar shape of the WFPC2 field, combined with the rotation angle, results in an orientation which is not determined by a target's coordinates, and may vary between observations of the same target. This makes it harder to plan composite, wide-field observations, such as the Groth Survey Strip, and wide field studies of galaxy clusters. Moreover, duplicate observations of the same pointings usually suffer from incomplete coverage of the field of view, unless scheduled at the same time of year.

All data obtained by *HST* are archived with, at most, a one-year proprietary period, after which they can be used freely and obtained through the Space Telescope Science Institute (STScI) data archive. The Time Allocation Committee does not approve proposals of duplicate observations as a part of the time allocation policy. Duplicate observations (i.e., observations with similar coordinates, same instrument and configuration and similar sensitivity) are performed only when the proposer provides scientific justification for the duplication (for example, conducting a variability study) or when re-imaging is necessary due to technical or scheduling problems detected during, or after, the first observation.

In this work, we have made extensive use of the *HST* archive to search for SNe. The disadvantages of using archival data are obvious. Each observation was executed under different specifications, which are not necessarily optimized for all kinds of research. Transient objects cannot be verified or followed up promptly after the observation. The data are not uniform, with respect to instrument configuration, exposure time and orientation. Nevertheless, in surveying well studied archival fields for SNe, we benefit by the availability of data (such as galaxy redshifts), which would have been time consuming to obtain otherwise.

2.2 Archival target selection

We have searched the *HST* archive for deep duplicate WFPC2 observations suitable for surveying for cluster and field SNe. In this work, we describe the analysis of two subsets of data: a sample of galaxy cluster fields, and the Groth Survey Strip data, which constitute a homogeneous non-cluster dataset.

For two WFPC2 observations to be considered duplicates, we required that they had been obtained through the same filter, and that the angular distance between their field centers was less than 75 arcsec. The requirement for identical filters is due to the need for accurate image subtraction when searching for faint transients. The angular separation criterion is driven by the peculiar shape of the WFPC2 field, coupled with the random *HST* orientations, which can result in observations that are nominally duplicate, but have little overlap area.

To optimize the search for SNe, especially at high z, where cosmological time-dilation is important, we required a minimal time separation between data sets of 30 days. The implications of this criterion are accounted for in the analysis of our results. Finally, we have limited our search to deep observations, with total exposure times of at least 2000 s in one of the broad-band *HST* filters. In order to facilitate reasonable rejection of cosmic rays and hot pixels, we required that at least one of the duplicate data sets consist of at least three sub-exposures. When both duplicate data sets had three or more sub-exposures, we searched for candidate variable objects in both. In cases where only one of the data sets was suitably split, the other set was used only as a reference, since the possibility of cosmic ray events mimicking transient objects could not be ruled out.

Cluster fields were identified as such by the target name, or, when the names were not revealing, by searching the NED database for known clusters near the field coordinates. The details of our final cluster sample are given in Table 2.1.

The non-cluster sample, i.e., the "Groth Survey Strip" (GSS, Groth et al. 1994), consists of 28 adjacent WFPC2 fields, at high Galactic latitude (l=96°, b=61°), covering a total area of $\sim$120 arcmin^2. The original objectives of the first epoch observation included analysis of galaxy clustering, measurement of galaxy counts, and measurement of the galaxy luminosity, color and morphology distribution. Each WFPC2 exposure was divided into four sub-exposures in each filter, with a total of 2800 in the F606W ("wide-V") filter, and 4400 sec in the F814W ("wide-I") filter. The individual pointings were oriented so that adjoining WFPC2 fields form a chevron pattern. There is an overlap of $\sim$0.44 arcmin^2 (0.28 of one chip) between each two neighboring pointings. An extensive analysis of this field was preformed by several researchers (e.g., Sarajedini et al. 1999, Im et al. 2002, Simard et al. 2002, Nelson et al. 2002), using both the *HST* observations and ground-based telescopes. Spectra of several hundred objects in these fields were obtained as part of the Deep Extragalactic Evolutionary Probe project (DEEP; Simard et al. 2002), and are now available online at the DEEP archive website (http://deep.ucolick.org/).

A second epoch observation of the GSS was executed, in order to search for candidate halo white dwarfs via their proper motion (Nelson et al. 2002). Whereas the first epoch was observed between March 7 and April 9, the second epoch was scheduled between May 29 and June 11, 2000, resulting in different orientations of the telescope (see § 2.1 for field orientation). Due to this scheduling error, the program was terminated after imaging only 13 of the original GSS fields. On March 2001, the program was resumed, with a total of 20 fields observed at the correct roll angle. Three additional images were obtained on March 2002. These observations form a third-epoch observation of the GSS (Table 2.2). Each WFPC2 exposure in the second and third epochs is divided into six non-integer dithered sub-exposures, with a total of 4200 sec in the F606W filter. Since the GSS is very homogeneous, the detection efficiency is similar in all fields, and limited by the non-dithered shallower 1994 epoch.

The total area useful for our SN survey (i.e., with two or more epochs covering the same sky area) is 62.3 arcmin^2 in the cluster sample, and 207.2 arcmin^2 in the non-cluster sample. The area calculation is affected by the different orientation between epochs, and a partial overlap between adjacent fields which exists in some of the mosaics. In Tables 2.1 and 2.2 we specify the effective area for each field.

The PC1-CCD data were not used in the analysis, due to their lower sensitivity and the small addition of area. Moreover, in many fields (including the GSS data), the area covered by this CCD is almost fully covered by other CCDs.

2.3 Data analysis

Sets of WFPC2 images at a given epoch were combined using software based mainly on the *DITHER* package (Fruchter & Hook, 1997) within IRAF [1]. A flexible, high-fidelity algorithm was used to reject cosmic-rays and hot/cold pixels, even in stacks with as few as three sub-exposures, allowing their use in this project. We explain this algorithm in Appendix A.

The combined images from two available epochs were registered, using a general geometrical transformation, calculated from the positions of ~ 20 compact galaxies or stars, visible at both epochs. The images were scaled according to their exposure times and subtracted, forming a difference image. The stable *HST* point-spread function (PSF) allows for good cancellation of almost all non-variable objects, as shown in an example in Fig. 2.3. Some low-level residuals remain in the difference images near bright stars and at the nuclei of the brightest galaxies. These residuals are unlikely to mimic real objects, since their suspect origin is evident from the images. However, the residuals near galactic nuclei limit the detection of nuclear variability in these galaxies, either SNe close to the nucleus or active galactic nuclei

[1] IRAF (Image Reduction and Analysis Facility) is distributed by the National Optical Astronomy Observatories, which are operated by AURA, Inc., under cooperative agreement with the National Science Foundation.

Table 2.1 Duplicate *HST* Observations

Field	z	Epoch (UT Start)	Exposure [ks]	Sub-frames	Filter	Program ID	Area[a] [arcmin^2]	Apparent SNe
Abell 2218	0.18	Mar 11 1999	8.4	12	F606W	7349	4.69	1
		Jan 13 2000	10.0	10	F606W	8500	4.69	-
Abell 1689	0.18	Jun 27 1996	2.0	2	F814W	6004	0	-
		Jun 19 1997	4.0	4	F814W	6004	4.69	-
		Jul 07 1997	4.6	4	F814W	5993	1.56	-
		Feb 24 2000	4.0	4	F814W	8546	1.56	-
AC114	0.31	Jan 06 1996	16.6	6	F702W	5935	1.28	-
		Oct 26 1997	15.6	6	F702W	7201	1.28	-
MS1512.4+3647	0.37	Mar 19 1996	6.3	9	F555W	6003	2.30	-
		Jun 20 1997	10.4	8	F555W	6832	2.30	-
MS2053.7−0449	0.58	Oct 23 1995	2.6	2	F814W	5991	0	-
		Sep 25 1998	3.2	3	F814W	6745	4.42	-
MS1054.4−0321	0.83	Mar 13 1996	15.6	6	F814W	5987	4.69	3
		May 29 1998	6.6	6	F814W	7372	4.69	-
CL1604+4304	0.89	Feb 25 1994	32.0	16	F814W	5234	3.97	1
		Feb 28 1995	32.0	16	F814W	5234	3.97	1
RXJ0848.6+4453	1.27	Mar 01 1999	13.9	5	F814W	6812	4.69	-
		Apr 15 1999	13.9	5	F814W	6812	4.69	-
CL1645+46	> 2.8	May 7 1997	6.0	12	F814W	6598	3.42	-
		Sep 30 1999	5.3	4	F814W	7342	3.42	-
Groth Survey		Mar 7 1994	2.8	4	F606W	5090	85.03	2
Strip			4.4	4	F814W	5090	0[b]	
		May 29 2000	4.2	6	F606W	8698	40.05	-
		Mar 9 2001	4.2	6	F606W	8698	71.43	2
		Mar 28 2002	4.2	6	F606W	8698	10.69	-

Notes:
[a] The overlap area is set to zero for data sets with fewer then three sub-exposures. These data sets are used only as references for searching for SNe at other epochs (§ 2.2).
[b] The I-band dataset of the GSS was not used in this survey.

Table 2.2 The Groth Survey Strip Dataset

Field name	Overlap Area[b] [arcmin^2]			
	1994	2000	2001	2002
FIELD-141810+523320[a]	2.91	2.91	···	···
FIELD-141816+523430[a]		···	···	···
FIELD-141823+523540[a]	4.69	···	4.69	···
FIELD-141527+520410	4.27	3.19	4.27	···
FIELD-141534+520520	4.27	3.19	4.27	···
FIELD-141540+520631	4.27	3.19	4.27	···
FIELD-141547+520741	4.27	3.19	4.27	···
FIELD-141553+520851	4.27	3.19	4.27	···
FIELD-141600+521001	4.27	3.19	4.27	···
FIELD-141606+521111	4.27	2.91	4.27	···
FIELD-141613+521222	4.27	···	4.27	···
FIELD-141619+521332	4.27	3.19	4.27	···
FIELD-141626+521442	4.27	2.91	4.27	···
FIELD-141632+521552	4.27	···	4.27	···
FIELD-141638+521702	4.27	···	4.27	···
FIELD-141645+521812		···	···	···
FIELD-141651+521922		···	···	···
FIELD-141658+522032		···	···	···
FIELD-141704+522142	3.56	2.91	···	3.56
FIELD-141711+522252	3.28	···	3.28	···
FIELD-141717+522402	3.28	···	3.28	···
FIELD-141724+522512		···	···	···
FIELD-141731+522622	3.56	3.19	···	3.56
FIELD-141737+522731	3.56	2.91	···	3.56
FIELD-141750+522951		···	···	···
FIELD-141757+523101	4.69	···	4.69	···
FIELD-141803+523211	4.27	···	4.27	···

'Inventory' of the fields in the original Groth Strip, and the matching fields from *HST* proposal 8698 imaged during 2000, 2001 and 2002.

Notes:

[a] *HST* name is not consistent with the coordinates, in both epochs. The coordinates of these three fields are $14^h15^m08.2^s$ $+52^\circ00'39''.2$, $14^h15^m14.6^s$ $+52^\circ01'49''.5$, and $14^h15^m21.0^s$ $+52^\circ02'59''.8$ respectively.

[b] Fields / epochs marked with " ··· " were not imaged.

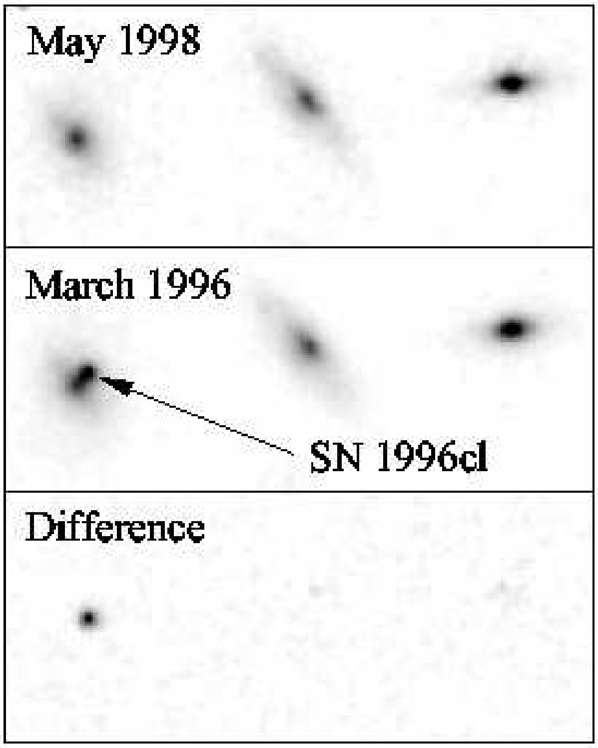

Fig. 2.2.— Example of image subtraction; SN 1996cl, in a galaxy in cluster MS1054.4−0321, in a $8''.5 \times 3''.6$ section of the difference image (lower panel) created by subtracting the data obtained in May 1998 (upper panel) from the data of the same field taken during March 1996 (middle panel). Note the clean subtraction of the galaxies, resulting from the stable *HST* point-spread function.

(AGN). This is taken into account by our detection efficiency simulations, described in § 4.

The difference images were methodically scanned by eye, and all residual objects checked and classified. After the elimination of obvious subtraction artifacts, the location of each residual object was checked in each of the sub-exposures from that epoch. For a candidate to be considered secure, we required that it have a stellar PSF, and appear in at least three independent subsets of the data, each consisting of the sum of individual exposures in which its location is not obviously affected by cosmic rays, with non-variable flux levels, to within errors. This criterion eliminates residual events consisting of cosmic rays that are coincident in several sub-exposures, as well as chip defects and rare, high amplitude, background fluctuations, since in these cases most of the candidate's flux in the final combined image comes from only some of the available sub-exposures.

Care was taken not to reject real events affected by cosmic ray hits, even in data sets with few sub-exposures. Real events could, in principle, be lost in three-image data sets if cosmic rays happened to hit the object's location on two of the three sub-exposures. However, given that only 1-2 per cent of the pixels in each image are affected by cosmic rays, this has a probability of $\sim 10^{-4}$, and much lower in data sets with more than three sub-exposures. Candidates that passed these criteria were considered real transient or variable sources, most likely high-z SNe (see § 5). In practice, all but one of the transient sources we found can be identified on each individual exposure, and not only in summed subsets. Figure 2.3 shows an example.

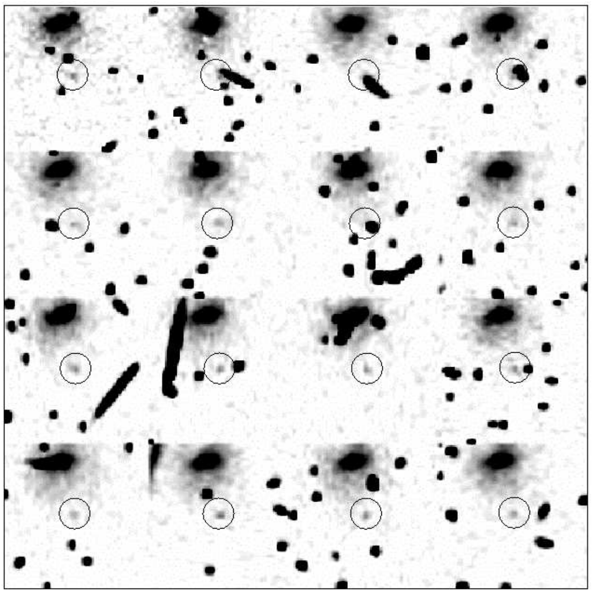

Fig. 2.3.— Example of candidate verification; $2\farcs1 \times 2\farcs1$ sections of the individual WFPC2 exposures at the location of SN 1995bf in CL1604+4304. The apparent SN is visible in all sub-exposures where the location is not affected by cosmic-ray hits, with a stellar PSF and constant flux, to within the expected errors.

In some of the fields (the 1994 epoch of the GSS and RXJ0848.6+4453), the rejection of hot pixels was almost impossible, since there was no dither between the sub-exposures. However, the PSF of bright sources is easily distinguished from hot pixels, thus enabling their detection. For fainter sources, we examined the same pixel in images of a different WFPC2 field, obtained just before or after the one in question, in order to identify the hot pixels.

The flux limit at each epoch depends on the length of the exposures and the filter used, and therefore varies between our sample fields, but in all sets the limit for > 50 per cent detection is better than $I_{814} = 26$ mag.

Chapter 3

Supernova Candidates

We have detected four SN candidates in the GSS data, and six apparent SNe in the cluster fields, including the rediscovery of SN 1996cl, which was previously known. For each SN, Table 3.1 lists the details, and Fig. 3 shows a section of the images at two epochs. As these objects are archival, our ability to categorize them is limited. Nevertheless, some information regarding their host galaxies is available from the literature. Among the ten SNe, eight are projected within 2.5 half-light radii of galaxies that are likely their hosts, while two have no obvious host (but see § 3.2). We have been able to determine the redshift and types of the host galaxies of five or six events from the literature (see below). We briefly discuss each SN below.

3.1 SN 1999gv in the field of Abell 2218

During March 1999, a large mosaic (22 positions) of WFPC2 images, covering the entire field of Abell 2218, was obtained through the F606W filter. The main goal of this program (PI Squires) was to create weak lensing shear maps, and to compare the resulting mass distribution to that derived via strong lensing, X-rays, and the Sunyaev–Zeldovich effect. In January 2000, following Space Shuttle servicing mission 3a, the cluster was re-imaged through the F450W, F606W, and F814W filters as an "early release" observation, intended to demonstrate the telescope performance. Comparison between the 8.4-ks F606W image from March 1999 and the 10.0-ks F606W image from January 2000, reveals a bright unresolved object in the 1999 exposure (Gal-Yam & Maoz 2000; see Fig. 3). The host galaxy is catalogued as No. 149 in Le Borgne et al. (1992), where it is classified as an elliptical galaxy with

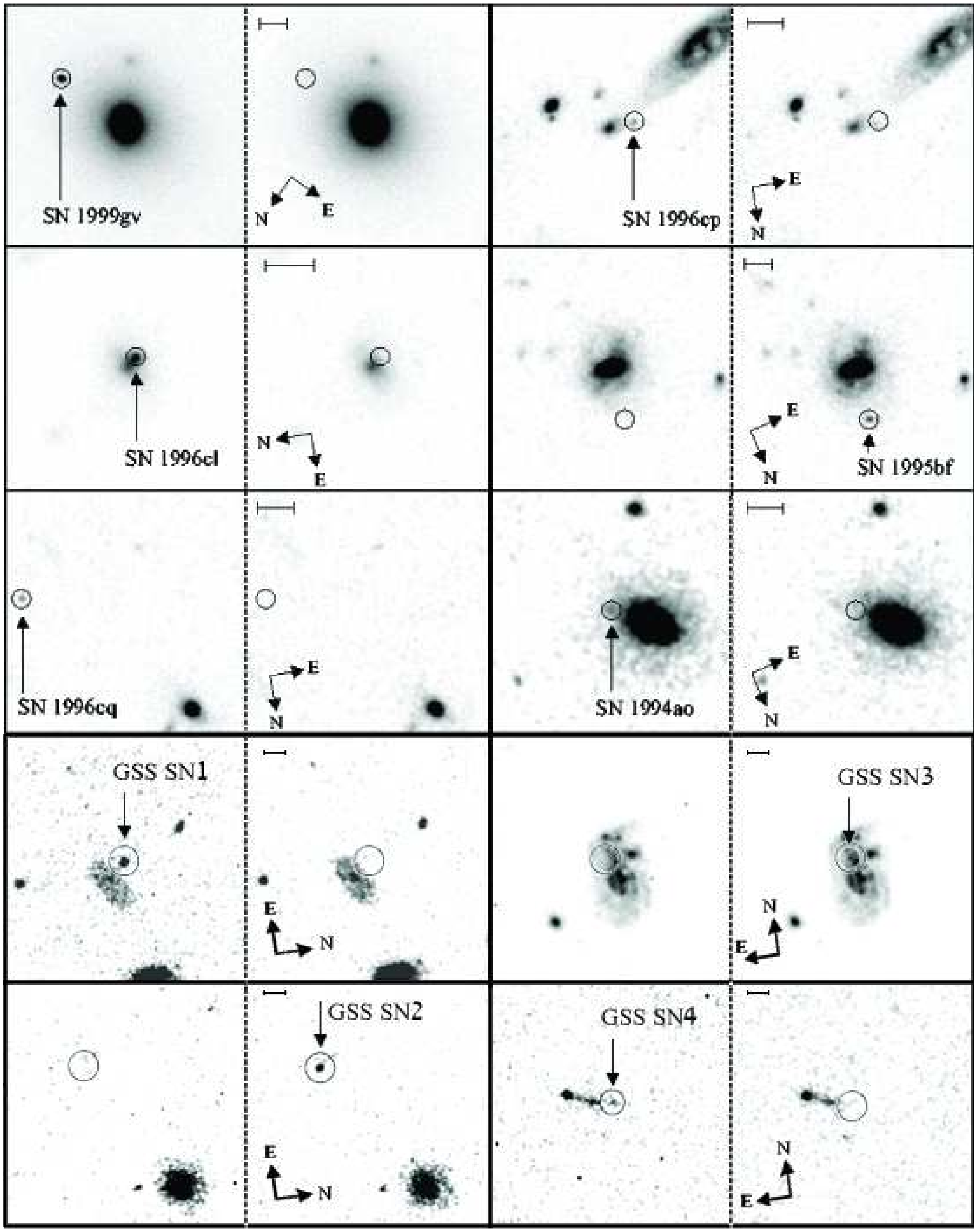

Fig. 3.1.— Sections of the images, at two epochs, for each of the ten apparent SNe. The scales shown in the upper-left-hand corners correspond to 1″.

$B = 19.9$ mag and redshift $z = 0.1753$. In view of the brightness of this SN, and its association with an elliptical cluster member, it is most likely a type-Ia SN in the cluster. Assuming a typical SN-Ia, the apparent magnitude suggests a SN age of ~ 25 days past maximum light.

3.2 SNe 1996cl, 1996cp, and 1996cq in the field of MS1054.4−0321

The core of the distant galaxy cluster MS1054.4−0321 ($z = 0.83$) was observed with the F814W filter during March 1996, in a program to study distant, X-ray selected clusters (PI Donahue). It was re-observed in May 1998, as part of a shallower, wide field mosaic (PI Franx), designed for a morphological large-scale study. A comparison of the images from the two epochs reveals three apparent SNe (Gal-Yam, Sharon, & Maoz 2001).

The brightest of the three is SN 1996cl, originally discovered by the SCP in ground-based data obtained on March 18, 1996 (Perlmutter et al. 1996), and spectroscopically confirmed as a type-Ia SN at the cluster redshift. In the *HST* observation, obtained 5 days prior to that of Perlmutter et al., the SN is detected with $I_{814} = 23.71$ mag, the magnitude expected for SN-Ia some 10 days (~ 5.5 days in the SN rest frame) before peak magnitude.

A second transient object in this field, SN 1996cq, is detected at $I_{814} = 25.61$ mag, without any obvious host galaxy. This object is superposed on a faint fuzz near the image detection limit that may be a low-surface-brightness galaxy associated with it.

The third transient source is SN 1996cp, with $I_{814} = 26.7$ mag. This object is superposed on a small knot of emission, 0.9 arcsec due east from the nucleus of a blue, late type galaxy with $z = 0.60$ (Milvang-Jensen et al. 2003). However, it could also be associated with a larger spiral galaxy that is found 4.1 arcsec to the south-east, cataloged as No. 1403 by van Dokkum et al. (2000), who classify it as a cluster member with $z = 0.81$. Since the emission knot which hosts SN 1996cp is closer to the $z = 0.60$ galaxy and has similar $I_{814} - V_{606}$ colors, we adopt a redshift of $z = 0.60$ for this SN. However, we cannot at this time exclude the possibility that the SN is associated with the nearby cluster galaxy (No. 1403) or that the emission knot is a separate galaxy altogether. Derivation of photometric redshifts for the emission knot hosting SN 1996cp from multi-color images of this cluster may shed more light on this issue.

3.3 SNe 1994ao and 1995bf in the field of CL1604+4304

The cluster CL1604+4304 ($z = 0.89$) was the target of a deep observation in 1994 (32 ks through the F814W filter; PI Westphal). However, a pointing error placed the target ~ 20 arcsec from the designated position. The cluster was therefore re-imaged one year later, again for 32 ks. Subtraction of these two deep images reveals two SNe (Gal-Yam et al. 2001). The first, SN 1995bf, with $I_{814} = 26.14$ mag, is found near a putative host, cataloged by Lubin et al. (1998) as No. 019, an Sb galaxy with $z = 0.985$, i.e., behind the cluster.

The limiting magnitude for SN detection in these particular images, derived from our detection-efficiency simulations (see § 4), is $I_{814} = 29$ mag, if the requirement that the SN appear in individual sets of sub-exposures is relaxed, to the effect that candidates need be detected with a stellar PSF and constant flux in only two independent subsets of the data. This analysis reveals a second, very faint, apparent SN in this cluster. SN 1994ao has $I_{814} = 28.4$ mag, near the detection limit, and is the faintest SN detected to date (~ 1.5 mag fainter than SN 1997ff; Gilliland et al. 1999; Riess et al. 2001). This object is near an S0 galaxy with $z = 0.496$, in the cluster foreground (No. 028 of Lubin et al. 1998). If the event is indeed associated with this host, it could imply it is a SN Ia, as core-collapse SNe (types II, Ib, Ic) are generally not found in S0 galaxies. However, the absence of core-collapse SNe in S0 galaxies has only been established in low redshift ($z \leq 0.1$) environments. If this is indeed a type-Ia SN, then the low luminosity implies it is many months past maximum. We report this event as an example of the capability of *HST* to find very faint SNe, but do not include it in our quantitative analysis of the results, below.

3.4 Four SN candidates in the Groth Survey Strip

Image subtraction of the three epochs in the GSS reveals four SN candidates. GSS SN1 candidate in FIELD-141527+520410 appears in an image obtained on Mar 8, 1994, and missing from the 2000 and 2001 epochs. It is identified as a star in the DEEP database (object No. 283_1832). Magnitudes were calculated for the two available filters – $V_{606} = 24.57$ mag, $I_{814} = 24.15$ mag.

Two candidates are detected in FIELD-141613+521222: GSS SN2, with $V_{606} = 25.5$, has no apparent host, and the faint ($V_{606} = 26.5$ mag) GSS SN3 is associated with a galaxy identified as galaxy No. 223_7474 in the DEEP database, which has no redshift information.

GSS SN4 is detected in the 1994 epoch of FIELD-141731+522622, associated with galaxy No. 092_6245 in the DEEP database, which has a photometric redshift $z = 1.45$. The SN is identified as No. 092_6444 in the DEEP database, with $V_{606} = 26.7$ mag and $I_{814} = 25.8$ mag. Assuming z=1.45, and the color estimates for high-z SNe presented by Reiss et al. (2003, Fig 2), we find that the colors and observed magnitude of this event are consistent with those of an exceptionally luminous Type II SN (similar to SN 1997cy) observed close to peak.

Table 3.1 Apparent Supernovae

SN	Field	Magnitude	α (2000)	δ (2000)	Offset from Host	Host z
1999gv	Abell 2218	$V_{606} = 21.64 \pm 0.03$	$16^h 36^m 02.2^s$	$+66^\circ 12' 34"$	$0''\!.8$ S $2''\!.8$ W	0.175
1996cl	MS1054.4−0321	$I_{814} = 23.71 \pm 0.04$	$10^h 56^m 59.1^s$	$-3^\circ 37' 36"$	$0''\!.1$ S $0''\!.05$ W	0.827
1996cq	MS1054.4−0321	$I_{814} = 25.61 \pm 0.05$	$10^h 57^m 02.2^s$	$-3^\circ 37' 34"$	-	?
1996cp	MS1054.4−0321	$I_{814} = 26.7 \pm 0.2$	$10^h 57^m 03.5^s$	$-3^\circ 37' 41"$	$0''\!.9$ E	0.596^a
1995bf	CL1604+4304	$I_{814} = 26.14 \pm 0.06$	$16^h 04^m 20.4^s$	$+43^\circ 04' 44"$	$2''\!.9$ N $0''\!.6$ W	0.985
1994ao	CL1604+4304	$I_{814} = 28.4 \pm 0.5$	$16^h 04^m 23.3^s$	$+43^\circ 03' 56"$	$1''\!.4$ S $1''\!.1$ W	0.496
GSS SN1	GSS (1994)	$V_{606} = 24.57 \pm 0.05$	$14^h 15^m 28.9^s$	$+52^\circ 04' 20.2"$	$0''\!.8$ N $0''\!.8$ E	
		$I_{814} = 24.15 \pm 0.05$				
GSS SN2	GSS (2001)	$V_{606} = 25.5 \pm 0.1$	$14^h 16^m 18.3^s$	$+52^\circ 12' 40.5"$	-	
GSS SN3	GSS (2001)	$V_{606} = 26.5 \pm 0.2$	$14^h 16^m 10.4^s$	$+52^\circ 12' 27.6"$	$0''\!.8$ S $0''\!.3$ W	
GSS SN4	GSS (1994)	$V_{606} = 26.7 \pm 0.2$	$14^h 17^m 22.1^s$	$+52^\circ 26' 38.8"$	$0''\!.7$ S $1''\!.8$ W	$1.45(?)^b$
		$I_{814} = 25.8 \pm 0.2$				

Notes:

[a] Other host galaxies possible, see text.

[b] Photometric redshift

Chapter 4

Detection efficiencies

We have carried out simulations in order to estimate our SN detection efficiencies. Several tens of artificial point sources ("fake" SNe) with known flux and the proper amount of Poisson noise were blindly added to the data for each field. The fake SNe were distributed such that the probability that a galaxy hosts a fake SN is proportional to the galaxy brightness. The separation of a SN from the galaxy centroid was chosen from a Gaussian distribution with σ equal to 0.85 times the galaxy's half-light radius. Thus, the fake-SN distribution follows the galactic light. Although in reality the SNe should follow the galactic *luminosity* in a given field, flux is a reasonable surrogate; the cluster galaxy population in a given field is all at a similar distance, and most of the field galaxies are likely also in a limited redshift range. Our procedure is also conservative, in the sense that it places the fake SNe on too-high galactic backgrounds, leading to an underestimate of the true efficiency, since cosmological surface-brightness dimming increases the contrast between a SN and its host-galaxy background at high redshifts. In principle, one might place some fake SNe at blank sky positions, to represent SNe in host galaxies that are below the detection limit (e.g., Gal-Yam et al. 2003). We find that our detection efficiency for such objects is significantly higher than for objects placed on galactic backgrounds. In line with our conservative approach, we did not include such events in the final simulations. The simulated data were reduced and searched for SNe, like the real data, and the fraction of recovered objects noted. In Figs 4.1 and 4.2, we plot our efficiency as a function of magnitude for each field.

Six of the nine clusters we discuss were observed through the F814W filter, which

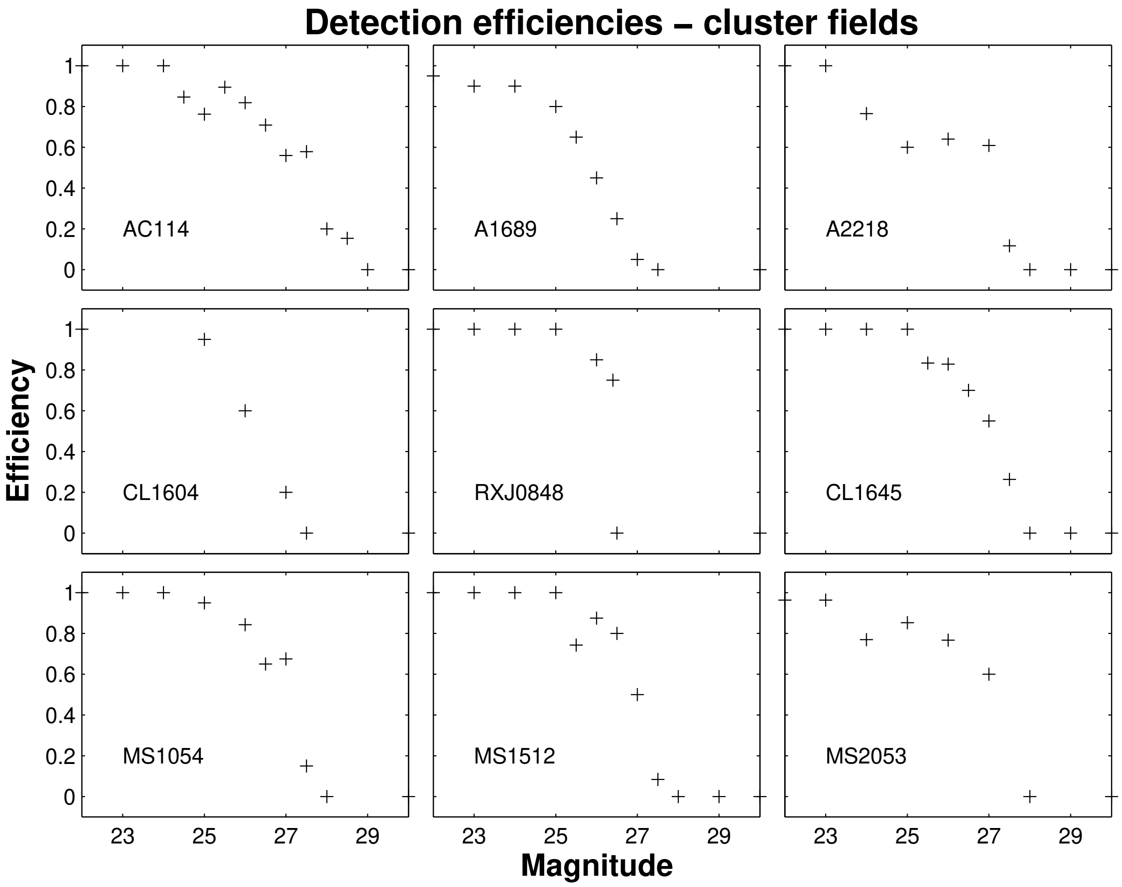

Fig. 4.1.— SNe-detection efficiencies as a function of magnitude for the cluster fields.

resembles the Kron–Cousins I filter. Model predictions for SN number counts in deep *HST* fields have been calculated for the I band (DF; S2000; see § 6), and for these fields the comparison is straightforward. However, the GSS fields and three of the cluster fields were imaged with other filters: F555W (Johnson V), F606W ("wide V"), and F702W ("wide R"; See Tables 2.1, 2.2).

A quantitative comparison of the observed V-band or R-band number counts with the expected I-band counts requires knowledge of the characteristic colors of the high-z SN population. While this information is fairly well known for type-Ia SNe (Perlmutter et al. 1999, Schmidt et al. 1998, Riess et al. 2001; 2003), beyond 25–26 mag, the counts are expected to be dominated by core-collapse SNe (e.g., DF; S2000). Broad-band photometry and spectroscopy of core-collapse SNe with $z > 0.5$, as well as UV spectra of local core-collapse SNe, for deriving K-corrections,

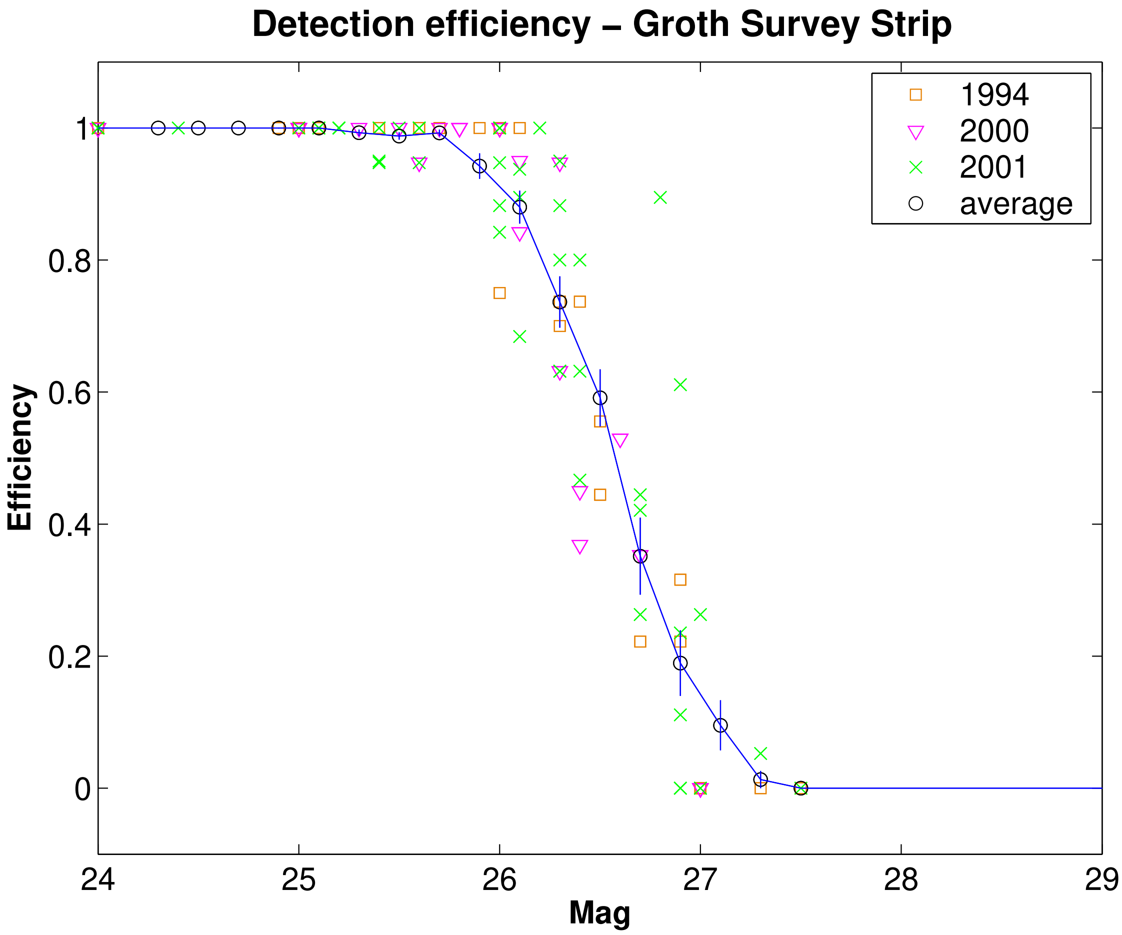

Fig. 4.2.— SNe-detection efficiencies as a function of magnitude for the GSS fields.

are scarce (DF; Gilliland et al. 1999; S2000). As the colors of SNe depend strongly on the SN redshift, type, age, and extinction, the color terms are highly model dependent. The relative fractions of the various sub-types of core-collapse SNe (II-P, II-L, IIn, Ib, and Ic) are observationally unknown at high-z, and must be assumed based on sparse data from local observations.

Following DF and S2000, we assume that about half of the type-II SNe are type II-P events. (The actual fraction of the various SN sub-types is controversial; we merely make the same assumptions as DF and S2000 in order to compare their models and our observations self-consistently). Based on UV spectra of local type-II SNe, DF assume that type II-P SNe show a strong UV deficit as they enter the plateau phase, some 20 days after maximum light, while type-II-L and -IIn SNe do not have this effect. At high z, the type II-P SNe will therefore have red $V - I$ and $R - I$ colors. We estimate that about half of the type II-P SNe are observed close to maximum light, when $V - I$ and $R - I$ are close to zero (Fig. 10 of DF), and apply no color correction to the efficiency for this fraction of the population. For the remaining type II-P SNe, observed at rest-frame ages $t \geq 20$ days, we adopt the colors calculated by DF, based on the SN models by Eastman et al. (1994). Converting the colors from Fig. 10 of DF to the magnitude system we use, we obtain $R_{702} - I_{814} = 0.75$ and $V_{555} - I_{814} \geq 2$. Since the F606W filter extends further into the red than F555W, and has significantly higher sensitivity, we assume $V_{606} - I_{814} = 1.5$. The detection efficiency, η, that applies to the half of the type II-P SN population with ages $t \geq 20$ days is the efficiency found for the observed (non-I_{814}) band, at a magnitude obtained by adding the color term.

In all but one of the data sets we have analyzed, the interval between epochs is ten months or longer, ample time for even the slowest SNe to vary significantly, even when time dilation at $z \sim 1$ is taken into account. The two epochs we compare in the case of RXJ0848.6+4453, however, are separated by only 44 days, equivalent to 22 rest-frame days for a $z = 1$ SN. Slowly-varying SNe IIn and SNe II-P during their plateau phase could become hard to detect in this data set. To correct for this possible bias, we again assume that about 1/2 of the high-z SNe we expect to discover are SNe II-P. These are expected to be in the slowly varying phase of their light curve for about 1/3 of the time they are observable. We therefore estimate that 1/6 of the expected high-z SNe would not be detected, and apply a correction of 5/6 to the core-collapse SN detection efficiency in this data set. One also needs to correct for the possibility that SNe observed on the rise in the first epoch would have approximately the same magnitude (within our observational error) when observed in the declining phase 44 days later, and thus avoid detection. Using simulated variable objects superposed on the actual images, we find that $I = 26$ objects can vary by 0.4 mag, at most, and still avoid detection. Applying this to typical light-curves for the various SN types, we estimate that about 15 per cent of the entire SN population might be lost. We therefore apply a further correction to our efficiency, with the final correction factor being $(5/6) \times 0.85 = 0.7$.

Chapter 5

Supernova alternatives

Apart from SN 1996cl, all the apparent SNe we discuss lack spectroscopic confirmation. We now consider alternative explanations, other than SNe, for the observed objects, and argue that all are unlikely.

Solar system objects – Small bodies in the Solar System (e.g., Kuiper Belt objects – KBOs; Trujillo, Jewitt & Luu 2001, and references therein) can potentially mimic transients. To pose as one of our apparent SNe, such an object must be faint ($I_{814} > 22$ mag) and slowly moving. However, the combination of relatively long observing periods (hours to days) with the *HST* resolution allows us to set firm upper limits on the proper motions of the detected transient events. For the relevant data set with the shortest observing period (MS1054.4−0321), the upper limit on the motion of the transients is $\mu \leq 0.12'' \mathrm{day}^{-1}$. For all fields in which we have found SN candidates, the expected parallaxes of a KBO at 50 AU, in the field directions and at the times of observation, as a result of the Earth's orbital motion, are $> 70'' \mathrm{day}^{-1}$. This is much larger than our upper limit. We note that the proper motion of a KBO at several tens of AU from the Sun cannot be large enough to offset the effect of the Earth's parallax, so that KBOs, regardless of their exact orbital parameters, cannot account for any of the events we discuss.

Variable Galactic stars – The fainter ($I_{814} \sim 26$ mag) among the transient events we have discovered are generally too faint to be plausible variable Galactic objects. Such objects would need to vary by at least ~ 1 mag in order to fall below the detection limit on one of the epochs. A chromospherically active $I = 27$ mag M4 dwarf (which, say, flared into our detection range), would be at a distance of

40 Kpc, far out in the low-stellar-density halo, and hence highly unlikely to turn up in such a small field. Cataclysmic variables in quiescence will always be brighter at minimum light than a single M-dwarf. Our only SN candidate brighter than $I_{814} = 25.5$ that lacks spectroscopic confirmation, SN 1999gv in Abell 2218, could be a bright flare from a Galactic G- or K-dwarf. However, the lack of any evidence for such flares at this position in numerous previous images of Abell 2218, obtained over several years through various telescopes (e.g., Gal-Yam & Maoz 2000), makes this possibility unlikely.

Variable stars in other galaxies – If the transient events we have found are associated with the galaxies near to which they are projected, then they are generally too luminous to be anything but SNe. Of the nine events we discuss, the redshifts of the probable hosts of five events are known (Table 3.1). The most luminous novae have absolute magnitudes $M_I = -11$ (Della Valle 1991; Warner 1995) and thus would be far too faint to be detected at the redshifts of these galaxies, falling below $I \sim 28.5$ mag at $z \sim 0.17$. The host galaxy of SN 1996cq is only marginally detected in the deep *HST* image. If this event is a nova, the implied luminosity of the host becomes implausibly low, $M_I > -8.7$ mag.

Active galactic nuclei – None of the events we discuss are located in the nuclei of the putative host galaxies, and hence are not Seyfert-like AGN. The candidates could, in principle, be more distant, highly variable quasars in the nuclei of undetected galaxies, projected by chance within < 2.5 half-light radii of the galaxies that are seen in five of six cases. By performing aperture photometry for all the galaxies in each image, we have determined the galaxies' half-light radii. We find that, even in the most crowded fields, < 5 per cent of the total area we have searched is within 2.5 half-light radii of a galaxy. For SN 1996cq, and one SN candidate in the GSS whose candidate hosts are barely detected, the quasar option cannot be ruled out as firmly.

Gamma-ray burst (GRB) afterglows – Recent observations of gamma-ray burst optical afterglows suggest that these explosions are not isotropic (e.g., Frail et al. 2001, and references therein). If the gamma rays are more beamed than the optical emission, there may be many optical afterglows that have no corresponding gamma-ray burst (Rhoads 1997). Such events could, in principle, explain some of the transients we have discovered. However, Dalal, Griest, & Pruet (2002) show that even a continuous monitoring campaign reaching a limiting magnitude of $R = 27$ is expected to yield < 0.15 events deg^{-2} yr^{-1}. Our search has visited a total area < 0.08 deg^2, only twice. Moreover, in view of recent studies of GRB afterglows (e.g., GRB 021211, Della Valle et al. 2003; GRB 030329, Stanek et al. 2003) which suggest an association of long-duration GRBs and core-collapse SNe this point may well become semantic.

We conclude that most or all of the events we have discovered are likely bona-fide SNe. Nevertheless, in our derivation of field counts, the estimated uncertainties account for the more ambiguous identifications of several of the candidates. In our comparisons of field counts to theoretical predictions (§ 6), if any of the events were not SNe, the discrepancy between observations and these models would only grow.

Chapter 6

Comparison with theoretical predictions

Prediction of the number of SNe detectable in a survey such as ours requires accounting for several factors. First, since core-collapse SNe follow the SFH (the progenitors are short lived), one can use a redshift-dependent SFH model as a proxy for the cosmic explosion rate. The normalization of this function is obtained by assuming an initial mass function and a miminum mass for core collapse (usually $8M_{\odot}$). The modeling of the SN Ia rate is more complicated, and requires knowledge of the delay time between star formation and explosions of the SN Ia progenitors. Given the SN rate (core collapse or Ia) as a function of redshift, the number density of observable SNe to a given limiting magnitude and redshift is calculated by summing all SNe which are more luminous than the detection limit, with each type of SN weighted by its fraction in the SN population. In order to determine, for each SN in this sum, whether it is above or below the detection limit, one needs to assume a typical form for the lightcurve of each type of SN, as well as the distribution of peak magnitude values. One can then calculate the time during which the SN flux is above a given detection limit. The intrinsic luminosity can be diminished, owing to dust obscuration in the host galaxy, with the latter depending on galaxy type, spatial orientation, and probably redshift. Finally, the *apparent* luminosity in a given band, which is the apparent spectrum multiplied by the response function of the filter, depends on redshift and cosmology, via K-corrections and luminosity distance.

We compare our observations with two such predictions, published by Dahlén & Fransson (1999; DF) and Sullivan et al. (2000; S2000). Both groups calculate the expected number of simultaneously detectable SNe in images with a number of different instruments, including *HST*, in order to predict the efficacy of high-z SN searches.

S2000 consider a search for SNe in deep, duplicate imaging of galaxy clusters by either WFPC2 or the ACS onboard *HST*. They first calculate the expected number of field (non-cluster) SNe, as a function of redshift. Then, they use this prediction and a gravitational-lensing model in order to quantify the effect of intermediate redshift galaxy clusters on the line of sight, for various mass profiles. In modeling the SN rates, S2000 consider two different SFHs, and examine two delay times (τ) between binary-system formation and SN Ia explosion. They adopt the models of Gilliland, Nugent, & Phillips (1999), which assume particular light-curve templates, K-corrections, luminosity functions, and peak-magnitude dispersions for SNe Ia and II. They find that the number counts depend weakly on the lensing and star-formation models they use (Table 1 of S2000). Background SN number counts are weakly affected by lensing, because the added depth given by the magnification is countered by the reduced effective area that is searched, due to that same magnification (Porciani & Madau 2000; S2000). We therefore adopt representative values from S2000 for the number of SNe expected per WFPC2 field for a two-epoch visit, given in their Table 1, for comparison with our cluster sample, as well as with the non-cluster fields. Converting the Vega-based magnitudes of S2000 (M. Sullivan, private communication) to AB magnitudes, their predicted counts are $N_p = 1.5$ SNe per WFPC2 field to $I_{814} \leq 26.4$ mag, and $N_p = 3$ SNe to $I_{814} \leq 27.4$ mag, in a bi-directional search (i.e., including SNe discovered in both epochs). S2000 assume 5.71 arcmin^2 for the area of a WFPC2 field, and therefore their predicted SN number density is $n_p = 0.16(0.32)$ arcmin^{-1} for $I_{814} \leq 26.4$ ($I_{814} \leq 27.4$) mag. Note that these numbers are for field SNe only, as S2000 exclude cluster events from their calculations.

In a similar work, DF have also calculated the numbers and properties of high-z SNe. DF present estimates for the expected number of observable SNe for *HST*, the planned James Webb Space Telescope (JWST), and ground-based instruments, in several broad-band filters. They include in their calculations light-curve and spectral evolution, and consider different cosmologies, SFHs and dust models. In their Fig.

9, they plot the expected number density of SNe to a given limiting magnitude. We note that DF calculated the expected SN number counts in blank (non-cluster) fields, but because of the weak effect of cluster lensing on total background counts, these predictions can be compared to our cluster-field observations as well.

Both groups find that the total number of SNe (i.e., of all types) per unit area doubles for every magnitude. At magnitudes $\lesssim 25$, depending on the SN Ia delay function, the counts are dominated by Ia's. However, by $I = 26$ mag, SN counts are dominated by core-collapse SNe, typically at $z \sim 0.7$.

Given a predicted SN surface density on the sky, we can calculate the expected number of SNe in our observed sample. For each data set, we determine the effective area, S, useful for SN search. This is just the sum of the areas that overlap the area of a reference epoch. For example, if useful data sets are available for two epochs with complete overlap, the effective area is just twice the illuminated area of the WF chips, or 9.38 arcmin^2. In cases where one of the epochs cannot be searched, and was used only as a reference, its contribution to the effective area is zero. The predicted SN count per magnitude interval, dm, per observed field is thus the surface density per magnitude interval, $n_p(m)dm$, times the fraction of a field effectively probed for SNe, times the search efficiency $\eta(m)$, with the latter modified by a color term for data sets that were not observed in the I band (see § 4):

$$n(m)dm = n_p(m) \times \frac{S}{9.38\mathrm{arcmin}^2} \times \eta(m, \mathrm{band})\ dm. \tag{6.1}$$

The total SN counts expected per field to a given limiting magnitude can be obtained by integrating Eq. 1 over m. In order to compare our results with the predictions of DF, we extracted the differential SN count density from their Fig. 9, for an $\Omega_m = 0.3$, $\Omega_\Lambda = 0.7$ CDM cosmology, and integrated Eq.(6.1) over magnitude. The cumulative number of SNe predicted to a limiting magnitude is plotted in Fig. 6.1.

S2000 list their results for the surface density of SNe, $N_p(< m)$, integrated up to some limiting magnitude, rather than the differential surface density $n_p(m)dm$. However, since the SN counts are a steeply rising function of magnitude, we can obtain a good approximation of the total by replacing the integral with the sum of two terms, for $I_{814} < 26.4$ mag and for $26.4 \leq I_{814} \leq 27.4$ mag, according to the cumulative numbers given by S2000, and weighted by $\eta(26.4)$ and $\eta(27.4)$, respectively. The effective areas, efficiencies, and predicted field SN numbers for each of the fields are given in Table 6.1.

A better approximation can be obtained for the GSS data, which have a very well-sampled efficiency function due to the homogeneity of the fields, under the following assumptions. First, since the predictions are not provided in differential form, we assume a surface density function whose integration agrees with the numbers provided by S2000. Based on Fig. 9 of DF, which approximately shows a power-law relation for $n_p(m)$ for limiting magnitudes up to ~ 27, and the results shown in Table 1 of S2000, we assume a power-law behavior of this function, with $N_p(< m + 1) = 2N_p(< m)$ for $m \sim 27$. Using the values given, we derive $n_p(m) = A \times 2^m$, with $A = 1.17 \times 10^{-8}$. Our detection efficiency function for the GSS fields can be parametrized as (see Fig. 4.1):

$$\eta(m) = \begin{cases} 1, & m \leq 26 \\ 27 - m, & 26 < m \leq 27 \\ 0, & 27 < m. \end{cases} \tag{6.2}$$

Integrating Eq. (6.1) over m, we get the predicted SN counts in the GSS to a chosen limiting magnitude (Table 6.1). These predictions are compared with our observations in Fig. 6.1.

We state our results with lower and upper confidence limits based on standard equations derived from Poisson statistics. The single-sided upper limits λ_u and lower limit λ_l are given by the probabilities

$$P(\leq n|\lambda_u) = 1 - \sum_{x=0}^{n} \frac{\lambda_u^x e^{-\lambda_u}}{x!} \ ; \quad P(\geq n|\lambda_l) = \sum_{x=0}^{n-1} \frac{\lambda_l^x e^{-\lambda_l}}{x!}.$$

Looking at Fig. 6.1, one sees that the counts predicted by S2000 are significantly higher than the observed values, and can be ruled out. However, the predictions of DF are marginally consistent with the observations. The observed numbers given in Table 5 are upper limits, since, however unlikely, some of the apparent SNe we discuss may not be SNe (§ 5). A comparison between the SN counts in the cluster and non-cluster fields, reveals a much higher SN-number density in the cluster fields. S2000 have shown that the lensing effects of the cluster hardly affect the SN counts and therefore we expect the number density of SNe to be similar, within the limitations of small number statistics. This suggests, that some of the events we counted as

Table 6.1 Predicted Field SN Counts – S2000

Field	Effective area (S)	Efficiency (η)		Expected SN number (N)	
	(arcmin^2)	$I = 26.4$	$I = 27.4$	$I \leq 26.4$	$I \leq 27.4$
Abell 2218	9.38	0.47^a	0	0.58	0.58
Abell 1689	7.81	0.29	0	0.30	0.30
AC 114	2.56	0.62^a	0.41^a	0.21	0.35
MS1512.4+3647	4.60	0.53^a	0	0.32	0.32
MS2053.7−0449	4.38	0.70	0	0.40	0.40
MS1054.4−0321	9.38	0.76	0	0.94	0.94
CL1604+4304	7.94	0.75	0.56	0.78	1.37
RXJ0848.6+4453	9.38	0.31^b	0	0.38	0.38
CL1645+46	6.84	0.72	0	0.65	0.65
GSS [c]	207.27			20.65	23.64
Total	269.5			25.21	28.92

Notes:

[a] Corrected with color term to convert to effective I-band efficiency (§ 4).

[b] Corrected to account for loss of slowly-fading SNe in data with short time interval between epochs (§ 4). There are no offsets between sub-frames of this data set, making the verification of faint ($I_{814} > 26.5$) point sources impossible. The efficiency for ($I_{814} > 26.5$) is therefore set to zero.

[c] The GSS efficiency was estimated with a continuous function (see text).

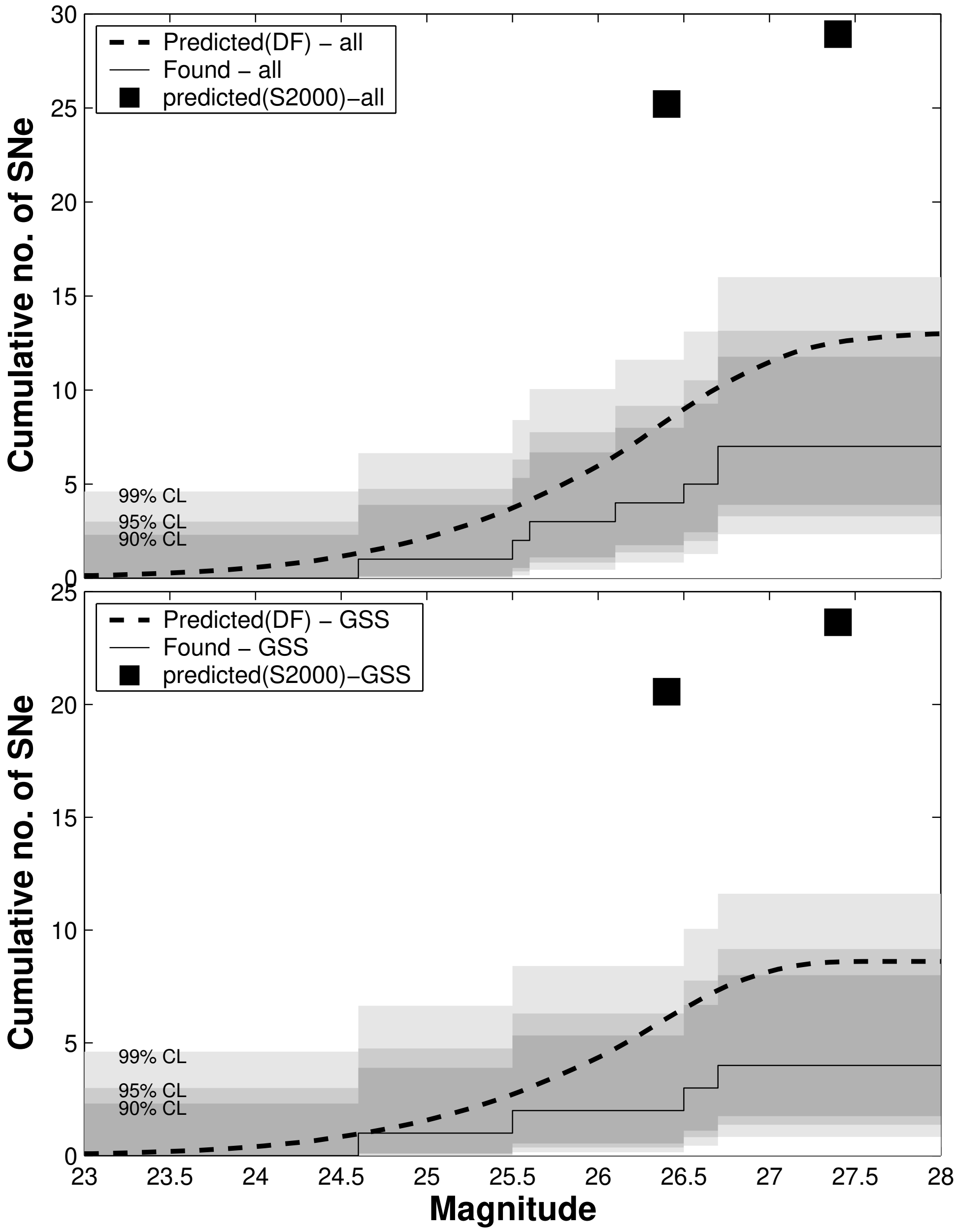

Fig. 6.1.— Cumulative number of SNe to limiting magnitude. Predictions of DF and S2000 are plotted in dashed lines and squares, respectively. The shaded areas represent 90%, 95% and 99% confidence levels of the observed numbers of SNe (solid line). In the lower panel, a subset of the data, including only the GSS fields.

Table 6.2 Observed vs. Predicted Field SN Counts

	S2000		DF	
	$N_p(m < 26.4)$	$N_p(m < 27.4)$	$N_p(m < 26)$	$N_p(m < 27)$
Groth Strip	20.65	23.64	4.81	8.29
Cluster fields	4.56	5.28	2.01	3.09
Total	25.21	28.92	6.82	11.38
Observed				
	$N(m < 26.4)$	$N(m < 27.4)$	$N(m < 26)$	$N(m < 27)$
Groth Strip	2	4	2	4
Cluster fields	2	3	1	3
Total	4	7	3	7

field events in the cluster sample (SNe 1996cp and 1996cq, for which the redshift is uncertain), may have been cluster events after all. If SNe 1996cp and 1996cq are, in fact, cluster events (§ 3.2), the difference between the prediction of DF and the data becomes statistically significant as well. Finally, (§ 4) our adopted efficiency values are likely underestimates, leading to too-low predictions.

It is instructive to investigate the sources of the differences between the predictions of S2000 and DF. The two groups assume very similar star-formation histories for the Universe (e.g., compare Figure 1 of DF with Figure 2 of S2000). Each group assumes somewhat different forms for the delay functions of SNe-Ia (i.e., the SN-Ia rate as a function of time after an initial burst of star formation), but at these magnitudes, Ia's are a small fraction, 15–25 per cent, of all SNe, so this has little effect on the total counts. For the UV spectrum of type-II-P SNe during their plateau phase, DF use a truncated blackbody model, while S2000 use an empirical spectrum, but their details are very similar, and in any case, this is of little consequence, since at $I < 27$ mag the median redshift of the SNe is $z \sim 0.7$, where the I band probes rest-frame ~ 4800 Å.

The bulk of the discrepancy between the predictions of S2000 and DF stems from two subtle differences in the treatment of type-II SNe, for which S2000 predict ~ 2 times more counts than DF. First, S2000 use a larger value for the dispersion of peak absolute magnitudes of type II-L SNe ($\sigma = 1.3$ mag), derived from the full sample of local type II-L SNe discussed by Miller & Branch (1990), and including the "overluminous" II-L SNe 1979C and 1980K. DF use a smaller dispersion ($\sigma = 0.5$)

derived from a sub-sample excluding the two overluminous SNe, but retain the (brighter) peak luminosity derived from the full II-L SN sample. The large dispersion chosen by S2000 results in a high-luminosity tail of type II-L SNe, a large number of which will be visible in a flux-limited SN search. Second, S2000 adopted a constant dust extinction value for all type-II SNe, of $A_V = 0.45$ mag, equivalent to $A_B = 0.66$ mag. DF used a minimum extinction value of $A_B = 0.32$ mag, lower than the one used by S2000, but modified it according to a random orientation of the host galaxy. This produced a large extinction for nearly edge-on hosts, with as many as 40 per cent of the core-collapse SNe suffering extinctions that are greater than 1 mag (T. Dahlén, private communication). This again, makes DF's SNe fainter than those of S2000, and the total predicted numbers lower.

Returning to our observational results, it appears that the combined assumptions of DF for the type-II SN peak magnitudes, dispersions, and dust extinctions are definitely a better description of the high-z SN population than those used by S2000. Of course, other variations on these assumptions can be devised, which may better fit the observed counts. Furthermore, some of the assumptions that are common to the models of both DF and S2000 could also be wrong, but counterbalanced by wrong SN-II parameters. With improved knowledge of the relative fraction of different SN types, their luminosity functions, and their spectra, the observed SN counts will be able to constrain some of the other parameters, such as the extinction of core-collapse SNe at high redshift.

Chapter 7

Summary and Future Work

We have conducted a search for SNe using data from deep observations of galaxy clusters and non-cluster fields from the *HST* archive, and have detected ten point-like transient events. Based on their observed characteristics and the known properties of different classes of variable objects, we have argued that most or all of these events are SNe. The redshifts and types of the likely host galaxies are available in the literature for five or six events, demonstrating the benefits of observing well-studied fields.

Folding in the observational parameters of our search, we have compared the numbers and magnitudes of the likely non-cluster (i.e., background or foreground) SNe we have found to published predictions of SN number counts. Such predictions depend strongly on a number of poorly known ingredients, and in particular the luminosity function and extinction of core-collapse SNe. The observed counts from our survey provide some initial constraints on these models. These counts, which are lower than the predictions of DF, and significantly lower than those of S2000, suggest that at $z \sim 0.7$, core-collapse SNe are relatively faint, due to either extinction or to a luminosity distribution without a high-luminosity tail.

Some of the assumptions of S2000 are obviously wrong, and the set of assumptions made by DF is only marginally consistent with the data. It is desirable to re-calculate these predictions using additional information on the parameters that has recently become available. Among such information is the peak brightness, lightcurve and abundance of type IIn SNe, recently reported by Hamuy (2003). It would also be interesting to test the effects of varying these parameters (e.g., the relative fractions and lightcurve distribution of sub-types of SNe within the SN population, the amount of obscuration by dust at high redshifts) that are currently unknown, in order to constrain them by observations.

This work shows that useful limits on high-z SN counts can be derived from repeated, deep *HST* imaging, even without any follow-up observations. Planned observations (rather than an archival search) would enable followup work that would reduce the systematic errors, and allow accurate determination of the SN types. We note that in our analysis we have not exploited the redshift information existing for some of the SNe, and this information can provide additional constraints (e.g., Gal-Yam & Maoz, 2003)

The current dominant source of uncertainty is the Poisson error due to small number statistics. Obviously, similar analysis of larger datasets would yield SN counts with higher precision. An example of such a dataset is the GOODS *HST* Treasury program, which was recently released. In this program, an area of approximately 320 square arcmin around the Chandra Deep Field South (CDF-S) and the Hubble Deep Field North (HDF-N) was surveyed by the ACS through four broad, non-overlapping filters: F435W (B), F606W (V), F775W (i), and F850LP (z). The images were taken at five epochs separated by $\sim$ 45 days, in order to search for SNe Ia at $1.2 < z < 1.8$ and test for the transition from cosmic deceleration to the acceleration predicted in models dominated by dark energy. Since the limiting magnitude for these observations, $I_{AB} \sim 27$, is close to our survey's typical detection limit, we can use our observed SN density to roughly estimate the number count of SNe of all types in the GOODS survey. The GOODS survey is $\sim$4.7 times larger than the total effective area we analyzed, and therefore we expect to find between $\sim$40-60 SNe with $I < 27$, in all five epochs. This is consistent with recent report by Strolger et al. (2003), of $\sim$40 SNe already found in this dataset. It is presently unclear to what degree the search is comprehensive, for all SN types at all stages, and to the faintest limits, but, the predictions of DF and S2000 lead to considerably larger numbers. We plan to analyze this and other new datasets in order to extend and improve upon the results obtained in the present work.

REFERENCES

Biretta, Lubin., et al. 2002, Hubble Space Telescope Call for Proposals, WFPC2 Instrument Handbook, Version 7.0 (Baltimore: STScI)

Cappellaro, E., Turatto, M., Benetti, S., Tsvetkov, D. Y., Bartunov, O. S., & Makarova, I. N. 1993, A&A, 268, 472

Cappellaro, E., Turatto, M., Tsvetkov, D. Y., Bartunov, O. S., Pollas, C., Evans, R., & Hamuy, M. 1997, A&A, 322, 431

Cappellaro, E., Evans, R., & Turatto, M. 1999, A&A, 351, 459

Dahlén, T. & Fransson, C. 1999, A&A, 350, 349 (DF)

Dalal, N., Griest, K., & Pruet, J. 2002, ApJ, 564, 209

della Valle, M. 1991, A&A, 252, L9

Della Valle, M. et al. 2003, A&A, 406, L33

Dimai, A. 2001, IAU Circ., 7719, 1

Eastman, R. G., Woosley, S. E., Weaver, T. A., & Pinto, P. A. 1994, ApJ, 430, 300

Filippenko, A. V. 1997, ARA&A, 35, 309

Foley, R. J. et al. 2003, PASP accepted, astro-ph/0307136

Frail, D. A. et al. 2001, ApJ, 562, L55

Fruchter, A. & Hook, R. N. 1997, Proc. SPIE, 3164, 120

Fruchter, A. S. & Hook, R. N. 2002, PASP, 114, 144

Galama, T. J. et al. 1998, Nature, 395, 670

Gal-Yam, A., & Maoz, D. 1999, in AIP Conf. Proc. 522, Cosmic Explosions, ed. S. S. Holt & W. W. Zhang (Melville: AIP), 107

Gal-Yam, A. & Maoz, D. 2000, IAU Circ., 7405, 2

Gal-Yam, A., Sharon, K., & Maoz, D. 2001, IAU Circ., 7700, 1

Gal-Yam, A., Maoz, D., & Sharon, K. 2002, MNRAS, 332, 37

Gal-Yam, A., Ofek, E. O., & Shemmer, O. 2002, MNRAS, 332, L73

Gal-Yam, A., Maoz, D., Guhathakurta, P., & Filippenko, A. V. 2003, AJ, 125, 1087

Gal-Yam, A., & Maoz, D., 2003, MNRAS submitted

Gal-Yam, A., 2003, PhD thesis, Tel Aviv University

Gilliland, R. L., Nugent, P. E., & Phillips, M. M. 1999, ApJ, 521, 30

Groth, E. J., Kristian, J. A., Lynds, R., O'Neil, E. J., Balsano, R., Rhodes, J., & WFPC-1 IDT 1994, Bulletin of the American Astronomical Society, 26, 1403

Hamuy (2003) in "Core Collapse of Massive Stars", Ed. C.L. Fryer, Kluwer, Dordrecht, astro-ph/0301006

Hardin, D. et al. 2000, IAU Circ., 7406, 2

Hatano, K., Branch, D., & Deaton, J. 1998, ApJ, 502, 177

Hubble, E. & Humason, M. L. 1931, ApJ, 74, 43

Im, M. et al. 2002, ApJ, 571, 136

Jorgensen, H. E., Lipunov, V. M., Panchenko, I. E., Postnov, K. A., & Prokhorov, M. E. 1997, ApJ, 486, 110

Le Borgne, J. F., Pello, R., & Sanahuja, B. 1992, A&AS, 95, 87

Leonard, D. C. et al. 2002, PASP, 114, 35

Li, W. D., et al. 1996, IAU Circ., 6379, 1

Lubin, L. M., Postman, M., Oke, J. B., Ratnatunga, K. U., Gunn, J. E., Hoessel, J. G., & Schneider, D. P. 1998, AJ, 116, 584

Madau, P., della Valle, M., & Panagia, N. 1998, MNRAS, 297, L17

Mannucci, F. & Ferrara, A. 1999, MNRAS, 305, L55

Maoz, D., 2003, & Gal-Yam, A.,MNRAS submitted

Milvang-Jensen, B., Aragón-Salamanca, A., Hau, G. K. T., Jørgensen, I., & Hjorth, J. 2003, MNRAS, 339, L1

Minkowski, R. 1941, PASP, 53, 224

Nelson, C. A., Cook, K. H., Axelrod, T. S., Mould, J. R., & Alcock, C. 2002, ApJ, 573, 644

Nomoto, K., Maeda, K., Mazzali, P. A., Umeda, H., Deng, J., & Iwamoto, K., 2003, To be published in "Stellar Collapse" (Astrophysics and Space Science; Kluwer) ed. C. L. Fryer, astro-ph/0308136

Pain, R. et al. 1996, ApJ, 473, 356

Pain, R. et al. 2002, ApJ, 577, 120

Perlmutter, S., et al. 1996, IAU Circ. 6621

Perlmutter, S. et al. 1997, ApJ, 483, 565

Perlmutter, S. et al. 1999, ApJ, 517, 565

Porciani, C. & Madau, P. 2000, ApJ, 532, 679

Qiu, Y. L. & Hu, J. Y. 2001, IAU Circ., 7753, 2

Reiss, D. J., Germany, L. M., Schmidt, B. P., & Stubbs, C. W. 1998, AJ, 115, 26

Riess, A. G. et al. 1998, AJ, 116, 1009

Riess, A., G., et al. 2003, ApJ accepted, astro-ph/0308185

Ruiz-Lapuente, P. & Canal, R. 1998, ApJ, 497, L57

Sadat, R., Blanchard, A., Guiderdoni, B., & Silk, J. 1998, A&A, 331, L69

Sarajedini, V. L., Green, R. F., Griffiths, R. E., & Ratnatunga, K. 1999, ApJS, 121, 417

Schaefer, B. E. 2000, IAU Circ., 7387, 1

Schmidt, B. P. et al. 1998, ApJ, 507, 46

Simard, L. et al. 2002, ApJS, 142, 1

Squires, G., Kaiser, N., Babul, A., Fahlman, G., Woods, D., Neumann, D. M., & Boehringer, H. 1996, ApJ, 461, 572

Stanek, K. Z. et al. 2003, ApJ, 591, L17

Strolger, L.-G., Riess, A. G., Dahlen, T., GOODS SN Searchers, & HHZS Team 2003, American Astronomical Society Meeting, 202, 25.05

Sullivan, M., Ellis, R., Nugent, P., Smail, I., & Madau, P. 2000, MNRAS, 319, 549 (S2000)

Sullivan, M. et al. 2003, MNRAS, 340, 1057

Tonry, J. L. 2003, ApJ, submitted, astro-ph/0305008

Tozzi, P. & Norman, C. 2001, ApJ, 546, 63

Treffers, R. R. et al., 1997, IAU Circ., 6627, 1

Trujillo, C. A., Jewitt, D. C., & Luu, J. X. 2001, AJ, 122, 457

van Dokkum, P. G., Franx, M., Fabricant, D., Illingworth, G. D., & Kelson, D. D. 2000, ApJ, 541, 95

Warner, B. 1995, "Cataclysmic Variable Stars", Cambridge Astrophysics Series, Cambridge, New York: Cambridge University Press, —c1995,

Zampieri, L., Pastorello, A., Turatto, M., Cappellaro, E., Benetti, S., Altavilla, G., Mazzali, P., & Hamuy, M. 2003, MNRAS, 338, 711

Zwicky, F., Humason, M. L., & Gates, H. S. 1960, AJ, 65, 504

Appendix A

Image Reduction Algorithm

One of the main challenges in searching for transients in *HST* images is avoiding false detections. CRs and hot pixels, if not dealt with carefully, appear like real astronomical objects, and mimic transient events. In this work, we have devised a high fidelity algorithm in order to produce clean, CR free, combined images. We explain the main principles of this algorithm below.

Composite, deep images are produced using the *drizzle* task within IRAF, developed by Fruchter and Hook (2002). This task is based on an algorithm, known as Variable-Pixel Linear Reconstruction (or informally as "drizzling"). *Drizzle* preserves photometry and resolution, can weight input images according to the statistical significance of each pixel, and removes the effects of geometric distortion both on image shape and photometry. It also compensates for the undersampling of the PSF (see § 2.1). Each WFPC2 detector is treated separately, thus enabling accurate photometry.

In order to effectively reject CRs, hot and cold pixels, we create a set of mask images, which indicate the location of pixels with bad data in each sub-exposure. To do this, we first create a reference image in the following manner. All sub-exposures of a given epoch are registered and shifted to the same position on the sky, using the *crossdriz*, *shiftfind* and *imshift* tasks within IRAF. The shifted sub-exposures are combined, creating a reference image, using the *imcombine* task.

In the combining process, the pixels corresponding to a certain location on the sky in all the shifted sub-exposures are sorted and compared, and a number of high and low value pixels are rejected. The number of pixels to reject depends on the number of sub-exposures and on the amount of CRs in them. The median of the remaining pixels is then used to compose the reference image. As the highest and lowest pixels, which include CRs and bad pixels are rejected, the resulting combined image is composed of pixels that best represent the emission from each part of the sky. Apart from rare cases where a given location in most, or all, of the sub-exposures is affected, the image is free from CRs, hot pixels and cold pixels. An additional difficulty arises when the image is not dithered, i.e., all sub-exposures are taken at the exact same coordinates. In such a case, only CRs are removed, but the rejection of hot or cold pixels is impossible.

The combined image created by the *imcombine* task, is relatively shallow, since the value of each pixel is determined from only a subset of the available sub-exposures. Therefore, this image is used only as a reference image, needed for the production of the set of mask images.

We create the set of mask images as follows. For each sub-exposure we measure the deviation from the reference image, by subtracting the reference image from the sub-exposure. Then, we divide the result by the reference image, in order to suppress high absolute residuals which are caused by statistical fluctuations in flux in the vicinity of sources, and which thus prevent their rejection. The resulting image is

$$D_i = \frac{[\mathrm{subexp}]_i - [\mathrm{ref}]_i}{[\mathrm{ref}]_i}, \tag{1}$$

where D denotes the relative deviation image, and i is a given pixel.

A histogram of such an image shows that the value of most of the pixels is close to zero, i.e., most of the pixels in a given sub-exposure are relatively close in value to the same pixels in the reference image. In the final image, we wish to exclude those pixels with large deviations from the reference image.

In order to do so, we select a range of allowed deviations (r), and set to unity the value of the pixels which are within that range. The value of the rest of the pixels is set to zero. The result is a mask image:

$$[\mathrm{mask}]_i = \begin{cases} 0, & D_i \leq -r \\ 1, & -r < D_i \leq r \\ 0, & D_i > r \end{cases} \tag{2}$$

The zero-value pixels in the outcome mask image indicate, for a given sub-image, the location on the chip of pixels which are too high or too low relative to the reference image, and are to be excluded in the final combining process.

Finally, all sub-exposures are drizzled to create the final image, with bad data points identified by *drizzle* by means of the zeroes in the mask images. The sub-exposures are weighted by their exposure time when necessary.

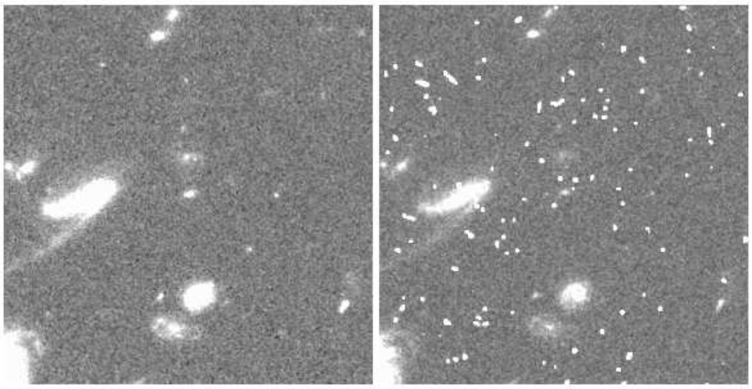

Fig. 1.— A 22″ × 22″ part of a drizzled, CR-free final image of HST FIELD-141613+521222 (left panel), and one of the sub-exposures of which it is composed (right panel), with many visible CRs.